EPJ Plus

Nuclear data activities at the n_TOF facility at CERN

The n_TOF Collaboration

Società Italiana di Fisica

Springer

Review

Nuclear data activities at the n_TOF facility at CERN[*]

The n_TOF Collaboration[**]

F. Gunsing[1,2,a], O. Aberle[2], J. Andrzejewski[3], L. Audouin[4], V. Bécares[5], M. Bacak[6], J. Balibrea-Correa[5],
M. Barbagallo[7], S. Barros[8], F. Bečvář[9], C. Beinrucker[10], F. Belloni[1], E. Berthoumieux[1], J. Billowes[11], D. Bosnar[12],
M. Brugger[2], M. Caamaño[13], F. Calviño[14], M. Calviani[2], D. Cano-Ott[5], R. Cardella[2], A. Casanovas[14],
D.M. Castelluccio[15,16], F. Cerutti[2], Y.H. Chen[4], E. Chiaveri[2], N. Colonna[7], M.A. Cortés-Giraldo[17], G. Cortés[14],
L. Cosentino[18], L.A. Damone[7,19], K. Deo[20], M. Diakaki[1,21], C. Domingo-Pardo[22], R. Dressler[23], E. Dupont[1],
I. Durán[13], B. Fernández-Domínguez[13], A. Ferrari[2], P. Ferreira[8], P. Finocchiaro[18], R.J.W. Frost[11], V. Furman[24],
S. Ganesan[20], A.R. García[5], A. Gawlik[3], I. Gheorghe[25], T. Glodariu[25], I.F. Gonçalves[8], E. González[5],
A. Goverdovski[26], E. Griesmayer[6], C. Guerrero[17], K. Göbel[10], H. Harada[27], T. Heftrich[10], S. Heinitz[23],
A. Hernández-Prieto[2,14], J. Heyse[28], D.G. Jenkins[29], E. Jericha[6], F. Käppeler[30], Y. Kadi[2], T. Katabuchi[31],
P. Kavrigin[6], V. Ketlerov[26], V. Khryachkov[26], A. Kimura[27], N. Kivel[23], M. Kokkoris[21], M. Krtička[9],
E. Leal-Cidoncha[13], C. Lederer[32,10], H. Leeb[6], J. Lerendegui[17], M. Licata[16,33], S. Lo Meo[15,16], S.J. Lonsdale[32],
R. Losito[2], D. Macina[2], J. Marganiec[3], T. Martínez[5], A. Masi[2], C. Massimi[16,33], P. Mastinu[34], M. Mastromarco[7],
F. Matteucci[35,36], E.A. Maugeri[23], A. Mazzone[7,37], E. Mendoza[5], A. Mengoni[15], P.M. Milazzo[35], F. Mingrone[16],
M. Mirea[25], S. Montesano[2], A. Musumarra[18,38], R. Nolte[39], A. Oprea[25], F.R. Palomo-Pinto[17], C. Paradela[13],
N. Patronis[40], A. Pavlik[41], J. Perkowski[3], I. Porras[2,42], J. Praena[17,42], J.M. Quesada[17], K. Rajeev[20], T. Rauscher[43,44],
R. Reifarth[10], A. Riego-Perez[14], M. Robles[13], P. Rout[20], D. Radeck[39], C. Rubbia[2], J.A. Ryan[11], M. Sabaté-Gilarte[2,17],
A. Saxena[20], P. Schillebeeckx[28], S. Schmidt[10], D. Schumann[23], P. Sedyshev[24], A.G. Smith[11], A. Stamatopoulos[21],
S.V. Suryanarayana[20], G. Tagliente[7], J.L. Tain[22], A. Tarifeño-Saldivia[22], D. Tarrío[13], L. Tassan-Got[4], A. Tsinganis[21],
S. Valenta[9], G. Vannini[16,33], V. Variale[7], P. Vaz[8], A. Ventura[16], V. Vlachoudis[2], R. Vlastou[21], A. Wallner[45],
S. Warren[11], M. Weigand[10], C. Weiss[2,6], C. Wolf[10], P.J. Woods[32], T. Wright[11], and P. Žugec[2,12]

1 CEA Saclay, Irfu, Gif-sur-Yvette, France
2 European Organization for Nuclear Research (CERN), Geneva, Switzerland
3 University of Lodz, Lodz, Poland
4 Institut de Physique Nucléaire, CNRS-IN2P3, Univ. Paris-Sud, Université Paris-Saclay, F-91406 Orsay Cedex, France
5 Centro de Investigaciones Energeticas Medioambientales y Tecnológicas (CIEMAT), Madrid, Spain
6 Technische Universität Wien, Vienna, Austria
7 Istituto Nazionale di Fisica Nucleare, Sezione di Bari, Bari, Italy
8 Instituto Superior Técnico, Lisbon, Portugal
9 Charles University, Prague, Czech Republic
10 Johann-Wolfgang-Goethe Universität, Frankfurt, Germany
11 University of Manchester, Manchester, UK
12 University of Zagreb, Zagreb, Croatia
13 University of Santiago de Compostela, Santiago de Compostela, Spain
14 Universitat Politècnica de Catalunya, Barcelona, Spain
15 Agenzia nazionale per le nuove tecnologie (ENEA), Bologna, Italy
16 Istituto Nazionale di Fisica Nucleare, Sezione di Bologna, Bologna, Italy
17 Universidad de Sevilla, Sevilla, Spain
18 INFN Laboratori Nazionali del Sud, Catania, Italy
19 Dipartimento di Fisica, Università degli Studi di Bari, Bari, Italy
20 Bhabha Atomic Research Centre (BARC), Mumbai, India
21 National Technical University of Athens, Athens, Greece
22 Instituto de Física Corpuscular, Universidad de Valencia, Valencia, Spain
23 Paul Scherrer Institut (PSI), Villingen, Switzerland
24 Joint Institute for Nuclear Research (JINR), Dubna, Russia
25 Horia Hulubei National Institute of Physics and Nuclear Engineering, Bucharest, Romania
26 Institute of Physics and Power Engineering (IPPE), Obninsk, Russia
27 Japan Atomic Energy Agency (JAEA), Tokai-mura, Japan
28 European Commission JRC, Institute for Reference Materials and Measurements, Retieseweg 111, B-2440 Geel, Belgium
29 University of York, York, UK

^{30} Karlsruhe Institute of Technology, Karlsruhe, Germany
^{31} Tokyo Institute of Technology, Tokyo, Japan
^{32} School of Physics and Astronomy, University of Edinburgh, Edinburgh, UK
^{33} Dipartimento di Fisica e Astronomia, Università di Bologna, Bologna, Italy
^{34} Istituto Nazionale di Fisica Nucleare, Sezione di Legnaro, Legnaro, Italy
^{35} Istituto Nazionale di Fisica Nucleare, Sezione di Trieste, Trieste, Italy
^{36} Dipartimento di Astronomia, Università di Trieste, Trieste, Italy
^{37} Consiglio Nazionale delle Ricerche, Bari, Italy
^{38} Dipartimento di Fisica e Astronomia, Università di Catania, Catania, Italy
^{39} Physikalisch Technische Bundesanstalt, Braunschweig, Germany
^{40} University of Ioannina, Ioannina, Greece
^{41} Universität Wien, Vienna, Austria
^{42} University of Granada, Granada, Spain
^{43} Centre for Astrophysics Research, University of Hertfordshire, Hertfordshire, UK
^{44} Department of Physics and Astronomy, University of Basel, Basel, Switzerland
^{45} Australian National University, Canberra, Australia

Abstract. Nuclear data in general, and neutron-induced reaction cross sections in particular, are important
for a wide variety of research fields. They play a key role in the safety and criticality assessment of nuclear
technology, not only for existing power reactors but also for radiation dosimetry, medical applications,
the transmutation of nuclear waste, accelerator-driven systems, fuel cycle investigations and future reactor
systems as in Generation IV. Applications of nuclear data are also related to research fields as the study
of nuclear level densities and stellar nucleosynthesis. Simulations and calculations of nuclear technology
applications largely rely on evaluated nuclear data libraries. The evaluations in these libraries are based
both on experimental data and theoretical models. Experimental nuclear reaction data are compiled on a
worldwide basis by the international network of Nuclear Reaction Data Centres (NRDC) in the EXFOR
database. The EXFOR database forms an important link between nuclear data measurements and the
evaluated data libraries. CERN's neutron time-of-flight facility n_TOF has produced a considerable amount
of experimental data since it has become fully operational with the start of the scientific measurement
programme in 2001. While for a long period a single measurement station (EAR1) located at 185 m from
the neutron production target was available, the construction of a second beam line at 20 m (EAR2) in
2014 has substantially increased the measurement capabilities of the facility. An outline of the experimental
nuclear data activities at CERN's neutron time-of-flight facility n_TOF will be presented.

1 Introduction

The generic notion "nuclear data" comprises the physical properties related to nuclear structure and nuclear reactions. Evaluated nuclear reaction data play an essential role in calculations and simulations for the design and operational studies of nuclear technology systems. For this purpose they have to contain all reactions and all energy regions, even where experimental data are missing, insufficient or inconsistent.

A nuclear data evaluation is the result of a complicated process involving a careful analysis of available existing, sometimes inconsistent experimental data sets combined with optimum theoretical models describing experimental data and providing data for gaps in experimental information. The outcome of this process is a single recommended and purposefully complete dataset, the evaluation. Both theoretical models and experimental data are the fundamental ingredients in evaluated data [1,2].

Nuclear data in general, and neutron-induced reactions in particular, are important for a number of research fields. In nuclear astrophysics, an intriguing topic is the understanding of the formation of the nuclei present in the universe and the origin of the chemical elements. Hydrogen and smaller amounts of He and Li were created in the early universe by primordial nucleosynthesis. Nuclear reactions in stars are at the origin of nearly all other nuclei. Most nuclei heavier than iron are produced by neutron capture in stellar nucleosynthesis [3–6]. Neutron-induced reaction cross sections also reveal the nuclear level structure in the vicinity of the neutron binding energy of nuclei [7,8]. The properties

---

* Contribution to the Focus Point on "Nuclear data for energy" edited by S. Leray.

** `www.cern.ch/ntof`
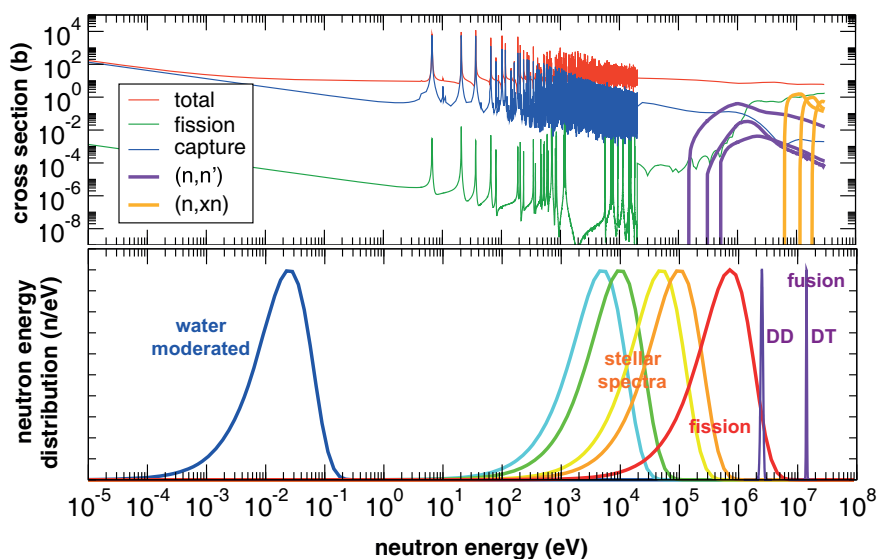
^{a} e-mail: `gunsing@cea.fr`

Fig. 1. Neutron-induced reaction cross sections for a typical heavy nucleus as a function of the neutron kinetic energy (upper panel), together with characteristic neutron energy distributions present in stellar environments and in technological applications like fission and fusion (lower panel). All distributions have been normalized to their maximum value.

of these levels are a crucial input to nuclear level density models. Finally, neutron-induced reaction cross sections are a key ingredient for the safety and criticality assessment of nuclear technology, including research on medical applications [9], radiation dosimetry, the transmutation of nuclear waste, accelerator-driven systems, future reactor systems as in Generation IV, and nuclear fuel cycle investigations [10–12].

Nuclear reaction data needed for such calculations are usually based on evaluated nuclear data libraries. Examples of such libraries are JEFF [13], ENDF [14], JENDL [15], CENDL, BROND and several others. While these libraries have started historically with a focus on nuclear technology applications, nowadays they are general-purpose libraries intended to be universal. For nearly any nuclear data application and simulation code, the content of an evaluated nuclear data library is not directly useable but needs to be processed to extract the needed information in a suitable format. For example neutron-induced reaction cross sections for resolved resonances are stored as R-matrix [16] resonance parameters, which is the most concise and fundamental way to represent this type of cross sections. From these parameters a reaction cross section can be calculated with the appropriate thermal broadening needed for an application. This Doppler-broadened cross section can then be merged with the energy range of smooth cross sections, and stored as interpolation tables, in order to obtain the reaction cross section over a wide energy range for a given temperature. Several special-purpose libraries with derived quantities exist as well. For example the database KADoNiS [17] is dedicated to Maxwellian averaged capture cross sections relevant for stellar nucleosynthesis. It contains data both calculated from evaluated nuclear data libraries and from experiments. The EXFOR data base [18] is the international storage and retrieval system for experimental results. It contains data that are often not available numerically in publications and laboratory reports. The observables including detailed experimental conditions have nowadays become the standard quality for submission.

Contributions to nuclear data come from a variety of experimental facilities including the pulsed white spallation neutron source n_TOF at CERN, which has been recently upgraded with its second beam line. Other neutron time-of-flight facilities comprise electron linac-based machines, like GELINA [19,20], IREN [21], KURRI [22], nELBE [23], ORELA (until recently) [24] and PNF [25], RPI [26], and proton-induced spallation targets similar to n_TOF, like MLF at J-PARC [27] and LANSCE [28]. All these facilities have their own unique and often complementary characteristics.

2 Nuclear reactions induced by neutrons

One of the most striking features of neutron-nucleus interactions is the resonance structure observed in the reaction cross sections at low incident neutron energies. Since the electrically neutral neutron has no Coulomb barrier to overcome, and has a negligible interaction with the electrons in matter, it can directly penetrate and interact with the atomic nucleus, even at very low kinetic energies of the order of electronvolts. At lower energies the De Broglie wavelength of the neutron becomes comparable to the size of interatomic distance of the target material and solid-state effects become important. The nuclear reaction cross sections can show variations of several orders of magnitude on

an energy scale of only a few eV. The origin of the resonances is related to the excitation of nuclear states in the compound nuclear system formed by the neutron and the target nucleus, at excitation energies lying above the neutron binding energy of typically several MeV. In fig. 1 the main reaction cross sections for a typical heavy nucleus are shown as a function of the energy. The reactions showing resolved resonances, typically elastic scattering, neutron capture, and for some nuclei fission, are clearly visible over a wide energy range. The position and extent of the resonance structure depend on the nucleus. Threshold reaction channels like (n, xn) or charged particle emission usually open up at higher energies. Also shown on the same energy scale in fig. 1 are several neutron energy spectra relevant for typical applications, normalized to give the same height. These spectra correspond to a Maxwell-Boltzmann distribution of the neutron velocities. On the low-energy side the neutron flux of a theoretical spectrum of fully moderated neutrons is shown. For an infinite water moderator at a temperature of about 293.6 K, the neutron density of this thermal spectrum shows a maximum at a speed of 2200 m/s corresponding to an energy of 25.3 meV. On the high-energy side the idealised neutron distribution of thermal-neutron induced prompt fission neutrons from ^{235}U is shown. Similar energy distributions are found for neutrons in certain stars where the synthesis of the nuclei heavier than about $A = 60$ takes place by neutron capture. For the s-process in Asymptotic Giant Branch stars, the neutrons originating mainly from ^{13}C(α, n) and ^{22}Ne(α, n) reactions, are present as a hot gas and with a Maxwellian kinetic energy distribution for temperatures with kT ranging from 5 to 100 keV.

Neutrons from fusion reactions, either from magnetic-confinement fusion with future applications of energy production or from inertial-confinement fusion have to be taken into account for issues related to shielding and activation. Reactions employed in most fusion developments are based on $D + T \rightarrow {}^4He + n$ (14.1 MeV) reactions (DT), as well as $D + D \rightarrow {}^3He + n$ (2.5 MeV) reactions (DD), which have quasi-mono-energetic energy spectra. Typical thermal fusion neutron spectra [29,30] at $T = 10$ keV are also shown in fig. 1.

3 The neutron time-of-flight facility n_TOF at CERN

The neutron time-of-flight facility n_TOF was constructed after an idea proposed by Rubbia *et al.* [31] and has become fully operational with the start of the scientific measurement programme in 2001 [32]. The facility is based on the 6 ns wide, 20 GeV pulsed proton beam from CERN's Proton Synchrotron (PS) with typically 7×10^{12} protons per pulse, impinging on a lead spallation target, yielding about 300 neutrons per incident proton. A layer of water around the spallation target moderates the initially fast neutrons down to a white spectrum of neutrons covering the full range of energies between meV and GeV.

The neutron bunches are spaced by multiples of 1.2 s, a characteristic of the operation cycle of the PS. This allows measurements to be made over long times of flight, and therefore low energies, without any overlap into the next neutron cycle. In this way it is possible to measure neutron energies as low as about 10 meV, and where the high-energy part of the neutron spectrum is free from slow neutrons from previous cycles. The large energy range that can be measured at once is one of the key characteristics of the facility.

Another important feature of n_TOF is the very high number of neutrons per proton burst, also called instantaneous neutron flux. In the case of radioactive samples in the neutron beam, this results in a very favourable ratio between the number of signals due to neutron-induced reactions and those due to radioactive decay events, which contribute to the background.

The neutron energy is determined by the time of flight technique. The neutrons, created at a time t_0, are guided through vacuum beam pipes to the experimental area at a distance L where they initiate reactions which are detected at time $t_0 + t$. The measured time of flight t of the neutron with mass m, together with the flight distance L, determines the neutron kinetic energy E_n using the energy-momentum relation with the neutron velocicy $v = L/t$ and momentum $p = \gamma m v$ as

$$E_n = E_{tot} - mc^2 = mc^2(\gamma - 1), \tag{1}$$

with $\gamma = (1 - v^2/c^2)^{-1/2}$ and where c is the speed of light. In reality, neutrons with a true energy E_n will be detected with a distribution in the measured velocities $v = L/t$ (the speed in the z-direction), determined by the measured time of flight t and flight path length L. Both t and L have distributions for a given energy E_n, related to the different effects of the time-of-flight method. By taking the derivative of eq. (1), the energy resolution ΔE is in first approximation related to the velocity resolution Δv as

$$\frac{\Delta E}{E} = \frac{\Delta v}{v}(\gamma + 1)\gamma. \tag{2}$$

This approximation is sufficient if the resolution components have a Gaussian distribution, each characterized for a given energy E_n by a single parameter ΔL and Δt, and hence Δv. The most important contributions to the resolution come from the time distribution of the impact of the proton pulse, the neutron transport in the target-moderator assembly and in the sample and detector, and the time resolution of the detector and electronics. In particular the resolution due to the target-moderator assembly is non-Gaussian and in addition highly asymmetric. Therefore the full probability density function of the velocity distribution, which is the spectrometer's response function, also known
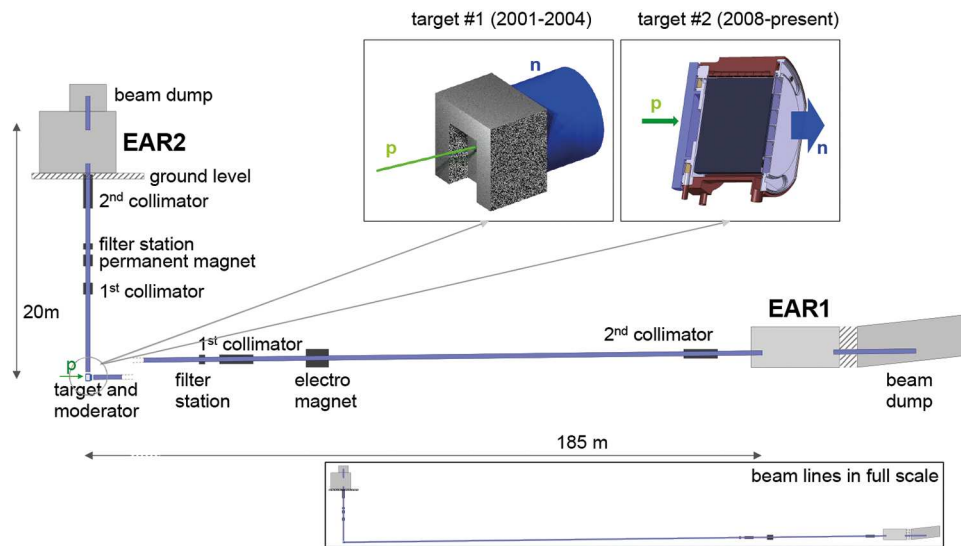
Fig. 2. Impression of the n_TOF facility with its two neutron beam lines (drawn in blue) ending in the experimental areas EAR1 and EAR2. The neutron source, on the left lower part of the drawing, is a lead spallation target surrounded by cooling water (the water is not shown on the insets). The incident proton beam with a nominal energy of 20 GeV, drawn in green, makes an angle of 10° in the horizontal plane. In the direction of EAR1 a separate neutron moderator is located. The two types of targets that have been used up to now are shown in the top inset. The horizontal neutron beam line has in reality a small angle of approximately 0.68° upwards. The picture where the placement of the beam elements are on scale, only shows the part of the long EAR1 beam line. On the inset below the main figure the full scale is shown.

as the resolution function (RF), needs to be used for a precise time-to-energy conversion. The RF not only broadens the resonances, but the asymmetry also shifts the peak positions in the reconstructed energy spectrum.

The RF is obtained in the entire energy range by simulations, and verified by measurements of well known narrow resonances. The full resolution function $R_E(E)$ of the reconstructed neutron kinetic energy E for a true energy E_n is by conservation of probability related to the distributions of time of flight R_t or equivalent distance R_L as

$$R_E(E)\mathrm{d}E = R_t(t)\mathrm{d}t = R_L(L)\mathrm{d}L, \tag{3}$$

where the distributions R are also dependent on the true neutron energy E_n. Usually components are converted into a single distribution depending on the use. While time-of-flight analyses require the resolution as R_t, the slow energy dependence of R_L makes it more useful for visualisations and interpolation. For the time-to-energy conversion of smooth cross section spectra it is sufficient to use the expectation value $\mathbb{E}\{L\}_{E_n} = \int L R_L \mathrm{d}L$, assuming that all resolution components are lumped into the normalized probability density R_L. This expectation value is also dependent on E_n.

For resolved resonances, this approximation is usually not sufficient and the full distribution needs to be convolved with the intrinsic shape of the resonances. The intrinsic resonance shape has in approximation a Breit-Wigner form depending on the reaction channel widths. The shape is altered by two broadening effects. First there is the Doppler broadening, related to the thermal motion of the target nuclei. This effect is well known. In good approximation, for metallic samples and many other cases this movement can be conveniently described by Gaussian broadening based on the free-gas model [33,34]. Cross sections are usually represented as Doppler broadened at a given temperature.

Two different target-moderator assemblies have been used up to now in the operation of n_TOF. During phase-I a first spallation target was used from 2001 up to 2004. The water coolant of the target also served as a neutron moderator. The spallation target was a block of lead of dimensions $80 \times 80 \times 60\,\mathrm{cm}^3$. During phase-II, after the installation in 2008 of an upgraded cylindrical lead spallation target 40 cm in length and 60 cm in diameter, the target was enclosed with a separate cooling circuit resulting in a 1 cm water layer in the beam direction, followed by an exchangeable moderator with a thickness of 4 cm. Demineralized water has been used as a moderator, as well as water with a saturated ^{10}B-solution in order to reduce the number of 2.223 MeV gamma rays from hydrogen capture, which otherwise forms an important contribution to the background due to in-beam gamma rays. The ^{10}B-loaded moderator, strongly suppressing thermal neutrons, affects the energy distribution of the neutron flux only noticeably below 1 eV.

Two beam lines are in operation today. In fig. 2 a sketch of the two beam lines is shown, together with two insets showing the two spallation targets used up to now. The corresponding neutron fluxes, per unit of lethargy, are shown in fig. 3. The strong suppression of the thermal neutron peak in EAR1 due to the ^{10}B-loaded moderator is clearly visible. The first neutron beam, collimated and guided through a nearly horizontal vacuum tube over a distance of
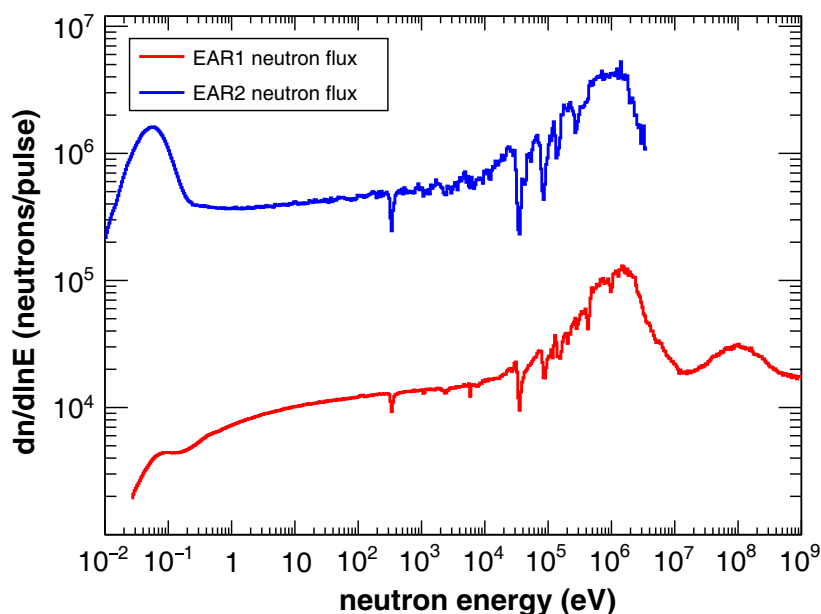
Fig. 3. The number of neutrons per equidistant logarithmic energy bin, *i.e.* per unit of lethargy, $(\mathrm{d}n/\mathrm{d}\ln E)$ per 7×10^{12} protons on target, referred to as "flux", integrated over the full Gaussian beam profile with a nominal FWHM of 18 mm in EAR1 and 21 mm in EAR2, as seen at the sample position at nominal distances of 185 m (EAR1) and 20 m (EAR2) for the small collimator. The shown fluxes are the preliminary results of several measurements and simulations [35, 36]. The strong reduction of the thermal peak in EAR1 is due to the ^{10}B-loaded moderator.

approximately 185 m, has been in use since the start of the facility in 2000. The beam line makes a small angle with the horizontal of approximately $0.68°$ upwards. It leads to an experimental area (EAR1) where samples and detectors can be mounted and neutron-induced reactions are measured. A more detailed description of the neutron source and EAR1 can be found in ref. [37] and references therein. Two pictures showing configurations of the experimental areas EAR1 and EAR2 are shown in fig. 4.

The second neutron beam line and experimental area (EAR2), has been constructed and has been operational since 2014. This flight path is vertical and about 20 m long, viewing the top part of the spallation target. In this case the cooling water circuit acts as a moderator. The vertical beam situation in the experimental area EAR2 necessitates adapated mechanical equipment to accommodate samples and detectors.

While the long flight path of EAR1 results in a very high kinetic-energy resolution, the short flight path of EAR2 has a neutron flux, which is higher than that of EAR1 by a factor of about 25. The energy distributions of the total number of neutrons at the sample plane, in this context called flux, are shown in fig. 3 for EAR1 and EAR2. The flux has a Gaussian beam-profile with a nominal full width at half maximum (FWHM) of 18 mm in EAR1 and 21 mm in EAR2 for the small collimator usually used for capture measurements. The higher flux opens the possibility for measurements on targets of low mass or for reactions with low cross section within a reasonable time. The shorter flight distance of about a factor 10 also has the consequence that the entire neutron energy region is measured in a 10 times shorter interval. For measurements of neutron-induced cross sections on radioactive nuclei this means 10 times less acquired detector signals due to radioactivity. Therefore the combination of the higher flux and the shorter time interval results in an increase of the signal-to-noise ratio of a factor 250 for radioactive samples, at cost of lower energy resolution. More details on EAR2 can be found in refs. [38, 39].

The n_TOF facility is also used for detector and electronic tests with a neutron beam, see for example ref. [40]. This type of tests is usually performed in the neutron beam dump in EAR1, without interfering with the physics programme.

3.1 Nuclear data measurements during phase-I (2001–2004)

A data acquisition system [41] based on Acqiris flash ADCs with 8 bit amplitude resolution and down to 1 ns sampling interval with 8 Mbytes of memory was developed and used during phase-I and phase-II. For each detector the full output signal from the start time given by the incident protons was recorded during the time window only limited by the internal memory. For the scintillator detectors, the digitizers were typically operated at 500 Msamples/s allowing the detector signal to be stored during a 16 ms long time-of-flight interval, corresponding to a minimum neutron energy

Fig. 4. Picture of the horizontal neutron beam line in EAR1 (left panel) showing the TAC in open position, and the vertical neutron beam line in the newly constructed EAR2 (right panel), showing a neutron capture setup with C_6D_6 detectors above the chamber containing the silicon neutron beam monitors (SiMon2).

of 0.7 eV. In order to reduce the amount of data, a zero-suppression technique was applied, after which the data was transferred to CERN's data storage facility CASTOR for off-line analysis with dedicated pulse shape analysis routines for each detector.

During the first phase from 2001 to 2004, data have been taken for a number of nuclides in capture and fission experiments. A list of measured nuclides and reactions together with the final or most relevant publication is given in table 1. Neutron capture measurements with C_6D_6 liquid scintillator gamma-ray detectors, which have a low sensitivity to scattered neutrons, were performed on the nuclei ^{24,25,26}Mg, ^{56}Fe, ^{90,91,92,94,96}Zr, ^{139}La, ^{151}Sm, ^{186,187,188}Os, ^{197}Au, ^{204,206,207,208}Pb and ^{209}Bi, and a first test measurement on ^{93}Zr. Gamma-ray cascades following neutron capture are for most nuclei extremely complex. In order to make the detection efficiency of a capture event independent of the cascade, the total-energy method using the so-called pulsed height weighting technique (PHWT) [42,43] is usually applied. Including the gamma-ray multiplicity of a typical cascade, the total detection efficiency for a capture event for the C_6D_6 detector setup is about 20%. In addition to slightly modified commercially available C_6D_6 detectors, two in-house developed deuterated benzene detectors were developed and used, containing a low-mass carbon fiber housing [44]. The capture samples were put in position by a remotely controlled carbon fiber sample changer [45].

A 4π total absorption calorimeter (TAC) consisting of 40 BaF_2 crystals was developed [82] and has been used for neutron capture measurements of ^{197}Au, ^{233}U, ^{234}U, ^{237}Np, ^{240}Pu, and ^{243}Am. The detection efficiency for this detector array approaches 100% and the gamma-ray energy resolution is much better than for C_6D_6 detectors, allowing a detection selectivity based on the total energy released in the capture cascade.

The relative neutron flux as a function of neutron energy is needed over the full energy range under investigation in order to obtain the unnormalized reaction yield. In addition to Monte Carlo simulations [83], in a dedicated measurement the neutron flux was measured with a ^{235}U loaded parallel plate fission ionization chamber from the Physikalisch-Technische Bundesanstalt in Braunschweig [32]. Furthermore, during the capture measurements the relative neutron flux was measured with the neutron monitor detector SiMon [84], consisting of an in-beam ^{6}Li deposit on a mylar foil and 4 off-beam silicon detectors for the detection of the ^{6}Li(n, ^{3}H)α reaction products. Up to 1 keV both methods are in good agreement, but at higher energies the flux obtained with the ^{6}Li(n, α) reaction depends on the applied corrections for the angular distribution of the α and triton particles.

Table 1. The measurements performed at n_TOF during phase-I from 2001–2004.

Nucleus	Reaction	Detector	ref.	Nucleus	Reaction	Detector	ref.
^{24}Mg	(n, γ)	C_6D_6	[46]	^{209}Bi	(n, γ)	C_6D_6	[65]
^{26}Mg	(n, γ)	C_6D_6	[46]	^{209}Bi	(n, f)	PPAC	[64]
^{90}Zr	(n, γ)	C_6D_6	[47]	^{232}Th	(n, γ)	C_6D_6	[66, 67]
^{91}Zr	(n, γ)	C_6D_6	[48]	^{233}U	(n, γ)	TAC	
^{92}Zr	(n, γ)	C_6D_6	[49]	^{233}U	(n, f)	FIC	[68, 69]
^{94}Zr	(n, γ)	C_6D_6	[50]	^{234}U	(n, γ)	TAC	
^{96}Zr	(n, γ)	C_6D_6	[51]	^{234}U	(n, f)	FIC	[70]
^{129}La	(n, γ)	C_6D_6	[52]	^{234}U	(n, f)	PPAC	[71, 72]
^{151}Sm	(n, γ)	C_6D_6	[53–55]	^{236}U	(n, f)	FIC	[73]
^{186}Os	(n, γ)	C_6D_6	[56, 57]	^{238}U	(n, f)	FIC/PPAC	[74, 75]
^{187}Os	(n, γ)	C_6D_6	[56, 57]	^{237}Np	(n, γ)	TAC	[76]
^{188}Os	(n, γ)	C_6D_6	[56, 57]	^{237}Np	(n, f)	FIC	[77]
^{197}Au	(n, γ)	C_6D_6/TAC	[58, 59]	^{237}Np	(n, f)	PPAC	[71]
^{204}Pb	(n, γ)	C_6D_6	[60]	^{240}Pu	(n, γ)	TAC	
^{206}Pb	(n, γ)	C_6D_6	[61, 62]	^{241}Am	(n, f)	FIC	[78]
^{207}Pb	(n, γ)	C_6D_6	[63]	^{243}Am	(n, γ)	TAC	[79]
^{208}Pb	(n, γ)	C_6D_6		^{243}Am	(n, f)	FIC	[80]
^{nat}Pb	(n, f)	PPAC	[64]	^{245}Cm	(n, f)	FIC	[81]

For capture experiments, the number of incident neutrons, measured with the flux detector over a surface larger than the beam spot, still has to be adjusted to the fraction of neutrons that are incident on the capture sample, referred to as the beam interception factor. The spatial neutron beam profile has been measured with a MicroMegas-based detector (MGAS) [85] and confirmed by simulations, allowing the energy-dependent beam-interception factor to be calculated.

The absolute normalization for capture measurements can be obtained if the measured cross section is known well enough in a particular energy region for the investigated nucleus or from a reference sample with a well-known cross section in the same measurement conditions. A related technique can be used with a sample thick enough to have a large total cross section ($n\sigma_T \gg 1$) in the peak of a resonance. This results in a so-called saturated resonance where in the vicinity of the resonance peak the capture yield is not proportional to the capture cross section $n\sigma_\gamma$ but to the ratio σ_γ/σ_T, independent of the sample thickness n. An example is the 4.9 eV resonance in ^{197}Au, which is saturated for a sample thickness of 0.1 mm. The particular shape of the capture yield near the saturated resonance allows the determination of the normalization with an R-matrix fitting code as explained in more detail for example in refs. [43, 86].

Fission cross section measurements usually use a stack of deposits among which are the nuclei ^{235}U or ^{238}U, which serve as cross section standards. Then a fission yield ratio is usually measured for an isotope rather than a fission yield. Fission ionisation chambers (FIC) were used to measure the fission cross sections. The chamber FIC-0 was used for the actinides ^{232}Th, ^{234}U, ^{236}U, and ^{237}Np relative to ^{235}U and ^{238}U. A similar detector, FIC-1, which was in addition suited for very radioactive samples (ISO-2919 compliant), was used to measure neutron-induced fission cross sections of the actinides ^{233}U, ^{241}Am, ^{243}Am, and ^{245}Cm, also relative to ^{235}U, ^{238}U. The third FIC chamber (FIC-2) was used for test measurements with ^{235}U and ^{238}U.

Fission detectors based on Parallel Plate Avalanche Counters (PPACs) were developed in addition. These fast detectors are used to identify fission by the simultaneous detection of both fission fragments, which allows to discard alpha and high-energy reactions. In this way they are capable of performing measurements up to 1 GeV. Furthermore, the position of each fission fragment is also measured, so the angle of the fragments with respect to the beam direction can be determined, allowing the study of the fission anisotropy. A stack of 10 PPACs interleaved with 9 targets was used in measurements of the fission cross sections of ^{nat}Pb, ^{209}Bi, ^{232}Th, ^{237}Np, ^{233}U, ^{234}U, relative to ^{235}U and ^{238}U.

Table 2. The measurements performed at n_TOF during phase-II from 2009–2012.

Nucleus	Reaction	Detector	ref.	Nucleus	Reaction	Detector	ref.
^{12}C	(n, p) activation	C_6D_6	[90, 91]	^{232}Th	(n, f) FFAD	PPAC	[89, 102]
^{25}Mg	(n, γ)	C_6D_6	[92, 93]	^{234}U	(n, f) FFAD	PPAC	[72]
^{33}S	(n, α)	MGAS	[94]	^{235}U	(n, f) FFAD	PPAC	[103]
^{54}Fe	(n, γ)	C_6D_6	[95]	^{235}U	$(n, \gamma)/(n, f)$	TAC/MGAS	[87]
^{56}Fe	(n, γ)	C_6D_6		^{235}U	(n, f)	PPAC	[104]
^{57}Fe	(n, γ)	C_6D_6	[95]	^{236}U	(n, γ)	C_6D_6	[105]
^{58}Ni	(n, γ)	C_6D_6	[96]	^{238}U	(n, f) FFAD	PPAC	[103]
^{59}Ni	(n, α)	CVD	[97]	^{238}U	(n, γ)	C_6D_6	[106]
^{62}Ni	(n, γ)	C_6D_6	[98]	^{238}U	(n, γ)	TAC	[107]
^{63}Ni	(n, γ)	C_6D_6	[99]	^{242}Pu	(n, f)	MGAS	[108]
^{87}Sr	(n, γ) spin	TAC	[100]	^{241}Am	(n, γ)	C_6D_6	[109]
^{92}Zr	(n, γ)	C_6D_6		^{241}Am	(n, γ)	TAC	[110]
^{93}Zr	(n, γ)	C_6D_6	[101]				

3.2 Nuclear data measurements during phase-II (2009–2012)

During phase-II from 2009–2012 the experimental area EAR1 has been upgraded to become a class A work zone, allowing to use unsealed radioactive samples. Several capture measurements were performed with the C_6D_6 scintillator gamma-ray detectors. The (n, γ) reaction on the light nucleus ^{25}Mg was investigated, as well as on enriched isotopes of iron (^{54}Fe, ^{56}Fe, ^{57}Fe), and of nickel (^{58}Ni, ^{62}Ni, ^{63}Ni), on the stable isotope ^{92}Zr, the radioactive ^{93}Zr, and on the nucleus ^{236}U. Capture reaction measurements on the actinides ^{238}U and ^{241}Am were performed with the two available capture detector systems: the C_6D_6 scintillators using the PHWT, and the TAC, the BaF_2 scintillator array using the total absorption method [82]. The TAC was also used in combination with a MicroMegas detector in a first attempt to measure the ^{235}U(n, γ) reaction using a veto on the ^{235}U(n, f) reaction [87]. An improved version of the MicroMegas neutron beam profile detector was used for the beam interception factor for the capture measurements [88]. An upgraded version of the PPAC assembly, with detectors tilted by 45 degrees in order to better control the efficiency of the system, was used to measure the angular distributions of ^{233}Th and ^{234}U fission fragments (FFAD) [89].

In addition to these measurements several other techniques have been tested at this facility. An experiment aiming at resonance spin assignments was performed on a ^{87}Sr sample. A first test measurement with a MicroMegas detector was done to perform fission cross section measurements on ^{240}Pu and ^{242}Pu. The results for the ^{240}Pu(n, f) experiment were not conclusive due to the high radioactivity of this nucleus, degrading the detector over time. This measurement was repeated in 2014 in the new EAR2, where the flux is much higher, allowing enough statistics to be collected in only a few weeks of measurement time.

A first test dedicated to an (n, α) measurement was investigated for the ^{33}S(n, α) reaction with a MicroMegas detector. Also this measurement was repeated later in EAR2 in 2015 to take advantage of the higher flux. A CVD diamond detector was used to measure the ^{59}Ni(n, α) cross section [97]. Finally the flux-integrated ^{12}C$(n, p)^{12}$B cross section, obtained by in-beam activation [90] was extracted. A list of the phase-II measurements and their references are given in table 2.

3.3 Nuclear data measurements during phase-III (from 2014)

During the planned long shutdown of CERN's accelerator complex from the end of 2012 to mid 2014, the construction of n_TOF's new second beam line and experimental area EAR2 [111] was performed and delivered by July 2014. The design was based on extensive Monte Carlo simulations with FLUKA [39] in order to optimize the beam line and collimation for a high neutron flux together with a minimized background. Additional simulations have been performed for data analysis purposes [112, 113]. In order to remove charged particles from the beam, a permanent 0.25 T magnet had to be installed since, unlike in the beamline for EAR1, there was no room for an electromagnet. Since then, the facility has been taking data in both the experimental area EAR1 (185 m horizontal flight path), and

Table 3. The nuclear data measurements performed at n_TOF during phase-III in 2014 and 2015 for both EAR1 and EAR2.

Nucleus	Reaction	Detector	EAR	ref.
^{7}Be	(n, α)	SILI	EAR2	[115, 129]
^{33}S	(n, α)	MGAS	EAR2	
^{70}Ge	(n, γ)	C_6D_6	EAR1	
^{73}Ge	(n, γ)	C_6D_6	EAR1	
^{74}Ge	(n, γ)	C_6D_6	EAR1	
^{76}Ge	(n, γ)	C_6D_6	EAR1	
^{147}Pm	(n, γ)	C_6D_6	EAR2	
^{171}Tm	(n, γ)	C_6D_6	EAR1, EAR2	
^{204}Tl	(n, γ)	C_6D_6	EAR1	
^{235}U	$(n, f)FF$	STEFF	EAR2	
^{237}Np	(n, f)	PPAC	EAR1	
^{240}Pu	(n, f)	MGAS	EAR2	[116]
^{242}Pu	(n, γ)	C_6D_6	EAR1	[117]

in the new EAR2 (20 m vertical flight path), using the neutron beams simultaneously produced by the same cylindrical lead spallation target as used in Phase-II. The experimental area EAR2 was designed as a class A work zone, allowing unsealed radioactive samples to be used, for which the n_TOF facility has particularly suited beam properties.

For the operation of phase-III, a new data acquisition system was developed, based on 175 MSample digitizers with a sampling frequency of up to 2 GHz and and amplitude resolution of 12, and recently also 14 bits. In addition to the higher-amplitude resolution, which was 8 bits with the previously used digitizers, the larger on-board memory has significantly increased the exploitable time-of-flight range which is now expanded down to thermal neutron energies.

A set of new in-house designed C_6D_6-based gamma-ray detectors entirely enveloped by a carbon fibre housing, as well as newly designed neutron flux detectors based on silicon detectors (SILI) [114] and MicroMegas detectors [88], were used for in-beam monitoring of the neutron flux and its energy dependency. In addition an XY-MicroMegas detector with 1 mm strips in both orthogonal directions together with dedicated electronics was developed to measure the neutron beam profile.

The measurement programme in EAR2 started with a first part of commissioning by measuring quantities such as flux and background and focusing on the feasibility of fission measurements. The energy dependence of the number of neutrons incident on the sample, referred to as the neutron flux, was measured both with an in-beam neutron-to-charged-particle converter foil, monitored by off-beam silicon detectors, and foils combined with in-beam MicroMegas detectors. The neutron converters consisted of nuclides with well-known cross sections as ^{6}Li(n, α), ^{10}B(n, α) and ^{235}U(n, f) in order to cover the energy dependence over a broad energy range. In fig. 3 the measured neutron fluxes in EAR1 and EAR2 are shown, based on an combined analysis of the available measurements [35, 36].

After the first part of commissioning, the very first physics measurement in EAR2 concerned the ^{240}Pu(n, f) reaction with MicroMegas detectors [116]. In 2015, the commissioning of EAR2 continued, exploring the possibilities of (n, γ) measurements, for applications in nuclear astrophysics [118] and nuclear technology, as well as neutron-induced charged particle reactions like the ^{7}Be(n, α) and an upcoming ^{7}Be(n, p) experiment. The complex multi-detector system STEFF [119] was installed in EAR2 for commissioning and a measurement of fission fragments spectroscopy on ^{235}U. A list of measurements during 2014 and 2015 and their references are given in table 3.

3.4 Further use of n_TOF measurements

The majority of the measurements at the n_TOF facility are related to cross sections: capture and fission experiments since phase-I and also (n, α) and (n, p) measurements in phase-II and phase-III. Once an experiment has been fully analysed and the results published, it is important to make the data available for further use. The basic measured data for a typical measurement are a set of detector count spectra as a function of neutron time of flight. Usually these spectra are then processed in order to obtain a reaction yield or cross section ratio. This is the quantity that is intended to be stored in the EXFOR database, which then subsequently can serve as a basis for nuclear data evaluations, which can

be adopted in new releases of evaluated nuclear data libraries. Applications for nuclear technology do not rely directly on measurements as collected in EXFOR, but nearly always on evaluated libraries. As an example of evaluations of neutron-induced reactions on ^{232}Th we mention ref. [120] for the resolved, and ref. [121] for the unresolved resonance region. The time path between a measurement and the inclusion in an evaluation for an evaluated nuclear data library is in general rather capricious. A list of requests for measurements is organized by the OECD-NEA High Priority Request List (HPRL) [122]. Evaluation efforts are performed in national projects or on an international scale like the CIELO project [123] for the nuclei ^{1}H, ^{16}O, ^{56}Fe, ^{235,238}U, and ^{239}Pu.

In the field of nuclear data much effort is nowadays put on reducing uncertainties. One strategy is to perform the same measurement at different facilities world-wide. Recognising and documenting measured data, uncertainties and covariances is an additional exertion in this respect. The process of reducing the several independent uncorrelated counting spectra to a single reaction yield or ratio as a function of time of flight (or neutron energy) introduces off-diagonal covariance elements. While the full covariance matrix of a yield consisting of several thousands of data points becomes too large to report directly in EXFOR, it is sometimes more convenient to use a vectorized covariance matrix reflecting the full data reduction process [124]. For smaller datasets on the contrary it is very instructive to access the full covariance matrix of a measured spectrum as for example nicely illustrated in refs. [125, 126]. Nevertheless, when the correlations introduced by the data reduction are small compared to certain common uncertainties, for example related to sample mass or normalization, it may be sufficient to report these uncertainties separately as "systematic" uncertainties. In any case, in order to make the data in EXFOR useful for evaluations, the description of the experimental details should be as complete as possible [127]. Data submission of n_TOF measurements to EXFOR, which is crucial for its consideration in evaluations, is an ongoing process. A comprehensive list of n_TOF data dissemination is maintained on [128].

Conclusion

The key features for accurate neutron measurements at the n_TOF facility with its two beam lines and experimental areas EAR1 and EAR2 are a large energy range, high neutron-energy resolution, and a high instantaneous neutron flux. EAR2 with its about 25 times higher flux than EAR1, combined with an additional reduction by a factor 10 of the background due to the sample's radioactivity, significantly enhances the possible measurements on unstable targets at n_TOF. The preparation and characterization of such targets suitable for neutron cross-section measurements is an increasingly complicated task, feasible only in highly specialized laboratories.

The measurements at CERN's neutron time-of-flight facility n_TOF with its unique features contribute substantially to our knowledge of neutron-induced reactions. This goes together with cutting-edge developments in detector technology and analysis techniques, design of challenging experiments, and training of a new generation of physicists working in neutron physics. This work has been actively supported since the beginning of n_TOF by the European Framework Programmes. One of the future developments currently being studied is a possible upgrade of the spallation target in order to optimize the characteristics of the neutron beam in EAR2. The n_TOF collaboration, consisting of about 150 researchers from 40 institutes, continues its scientific programme in both EAR1 and EAR2, in this way continuing its 15 years history of measuring high-quality neutron-induced reaction data.

References

1. Nicolas Alamanos *et al.*, Eur. Phys. J. A **51**, 12 (2015).
2. Pavel Oblozinsky, Nucl. Data Sheets **131**, iii (2016) DOI: 10.1016/j.nds.2015.12.001.
3. G. Wallerstein *et al.*, Rev. Mod. Phys. **69**, 995 (1997).
4. S.E. Woosley *et al.*, Nucl. Phys. A **718**, 3C (2003).
5. F. Kappeler *et al.*, Rev. Mod. Phys. **83**, 157 (2011).
6. T. Rauscher, AIP Adv. **4**, 041012 (2014).
7. T. von Egidy *et al.*, Phys. Rev. C **73**, 049901 (2006).
8. H.A. Weidenmuller *et al.*, Rev. Mod. Phys. **81**, 539 (2009).
9. S.M. Qaim, J. Radioanal. Nucl. Chem. **305**, 233 (2015).
10. G. Aliberti *et al.*, Nucl. Sci. Eng. **146**, 13 (2004).
11. A. Nuttin *et al.*, Prog. Nucl. Energy **46**, 77 (2005).
12. A. Nuttin *et al.*, Ann. Nucl. Energy **40**, 171 (2012).
13. A.J. Koning *et al.*, J. Korean Phys. Soc. **59**, 1057 (2011).

14. M.B. Chadwick *et al.*, Nucl. Data Sheets **112**, 2887 (2011).
15. K. Shibata, J. Nucl. Sci. Technol. **50**, 449 (2013).
16. A.M. Lane *et al.*, Rev. Mod. Phys. **30**, 257 (1958).
17. I. Dillmann *et al.*, KADoNiS v0.3, http://www.kadonis.org (2009).
18. N. Otuka *et al.*, Nucl. Data Sheets **120**, 272 (2014).
19. P. Schillebeeckx *et al.*, Nucl. Data Sheets **119**, 94 (2014).
20. W. Mondelaers *et al.*, Notiziario **11**, 19 (2006).
21. J. Adam *et al.*, Kerntechnik **70**, 127 (2005).
22. Masahiro Hino *et al.*, Nucl. Instrum. Methods A **797**, 265 (2015).
23. J. Klug *et al.*, Nucl. Instrum. Methods A **577**, 641 (2007).
24. K.H. Guber *et al.*, J. Korean. Phys. Soc. **59**, 1685 (2011).
25. Taofeng Wang *et al.*, Nucl. Instrum. Methods Phys. Res. B **268**, 106 (2010).
26. Y. Danon *et al.*, Nucl. Instrum. Methods A **352**, 596 (1995).
27. K. Kino *et al.*, Nucl. Instrum. Methods Phys. Res. Sect. A **736**, 66 (2014).
28. R.C. Haight *et al.*, Nucl. Data Sheets **123**, 130 (2015).
29. H. Brysk, Plasma Phys. Control. Fusion **15**, 611 (1973).
30. J. Eriksson *et al.*, Comput. Phys. Commun. **199**, 40 (2016).
31. C. Rubbia *et al.*, Technical report (1998).
32. C. Borcea *et al.*, Nucl. Instrum. Methods Phys. Res. Sect. A **513**, 524 (2003).
33. W.E. Lamb, Phys. Rev. **55**, 190 (1939).
34. D.G. Naberejnev *et al.*, Nucl. Sci. Eng. **131**, 220 (1999).
35. M. Barbagallo *et al.*, Eur. Phys. J. A **49**, 1 (2013).
36. M. Barbagallo *et al.*, in preparation (2016).
37. C. Guerrero *et al.*, Eur. Phys. J. A **49**, 27 (2013).
38. C. Weiß *et al.*, Nucl. Instrum. Methods A **799**, 90 (2015).
39. S. Barros *et al.*, J. Instrum. **10**, P09003 (2015).
40. Eleni Aza *et al.*, Nucl. Instrum. Methods A **806**, 14 (2016).
41. U. Abbondanno *et al.*, Nucl. Instrum. Methods Phys. Res. Sect. A **538**, 692 (2005).
42. J.L. Tain *et al.*, J. Nucl. Sci. Technol. **39**, 689 (2002).
43. A. Borella *et al.*, Nucl. Instrum. Methods Phys. Res. Sect. A **577**, 626 (2007).
44. R. Plag *et al.*, Nucl. Instrum. Methods Phys. Res. Sect. A **496**, 425 (2003).
45. P.M. Milazzo *et al.*, Nucl. Instrum. Methods Phys. Res. Sect. B **213**, 36 (2004).
46. C. Massimi *et al.*, Phys. Rev. C **85**, 044615 (2012).
47. G. Tagliente *et al.*, Phys. Rev. C **77**, 035802 (2008).
48. G. Tagliente *et al.*, Phys. Rev. C **78**, 045804 (2008).
49. G. Tagliente *et al.*, Phys. Rev. C **81**, 055801 (2010).
50. G. Tagliente *et al.*, Phys. Rev. C **84**, 015801 (2011).
51. G. Tagliente *et al.*, Phys. Rev. C **84**, 055802 (2011).
52. R. Terlizzi *et al.*, Phys. Rev. C **75**, 035807 (2007).
53. U. Abbondanno *et al.*, Phys. Rev. Lett. **93**, 161103 (2004).
54. S. Marrone *et al.*, Nucl. Phys. A **758**, 533C (2005).
55. S. Marrone *et al.*, Phys. Rev. C **73**, 034604 (2006).
56. K. Fujii *et al.*, Phys. Rev. C **82**, 015804 (2010).
57. M. Mosconi *et al.*, Phys. Rev. C **82**, 015802 (2010).
58. C. Massimi *et al.*, Phys. Rev. C **81**, 044616 (2010).
59. C. Lederer *et al.*, Phys. Rev. C **83**, 034608 (2011).
60. C. Domingo-Pardo *et al.*, Phys. Rev. C **75**, 015806 (2007).
61. C. Domingo-Pardo *et al.*, Phys. Rev. C **76**, 045805 (2007).
62. C. Domingo-Pardo *et al.*, J. Phys. G **35**, 014020 (2008).
63. C. Domingo-Pardo *et al.*, Phys. Rev. C **74**, 055802 (2006).
64. D. Tarrio *et al.*, Phys. Rev. C **83**, 044620 (2011).
65. C. Domingo-Pardo *et al.*, Phys. Rev. C **74**, 025807 (2006).
66. G. Aerts *et al.*, Phys. Rev. C **73**, 054610 (2006).
67. F. Gunsing *et al.*, Phys. Rev. C **86**, 019902 (2012).
68. M. Calviani *et al.*, Phys. Rev. C **80**, 044604 (2009).
69. F. Belloni *et al.*, Eur. Phys. J. A **47**, 2 (2011).
70. D. Karadimos *et al.*, Phys. Rev. C **89**, 044606 (2014).
71. C. Paradela *et al.*, Phys. Rev. C **82**, 034601 (2010).
72. E. Leal-Cidoncha *et al.*, Nucl. Data Sheets **119**, 42 (2014).
73. R. Sarmento *et al.*, Phys. Rev. C **84**, 044618 (2011).
74. C. Paradela *et al.*, Phys. Rev. C **91**, 024602 (2015).
75. M. Diakaki *et al.*, EPJ Web of Conferences **111**, 02002 (2016).
76. C. Guerrero *et al.*, Phys. Rev. C **85**, 044616 (2012).

77. M. Diakaki *et al.*, Phys. Rev. C **93**, 034614 (2016).
78. F. Belloni *et al.*, Eur. Phys. J. A **49**, 2 (2013).
79. E. Mendoza *et al.*, Phys. Rev. C **90**, 034608 (2014).
80. F. Belloni *et al.*, Eur. Phys. J. A **47**, 160 (2011).
81. M. Calviani *et al.*, Phys. Rev. C **85**, 034616 (2012).
82. C. Guerrero *et al.*, Nucl. Instrum. Methods A **608**, 424 (2009).
83. U. Abbondanno *et al.*, Technical Report CERN-SL-2002-053 ECT (2003).
84. S. Marrone *et al.*, Nucl. Instrum. Methods Phys. Res. Sect. A **517**, 389 (2004).
85. J. Pancin *et al.*, Nucl. Instrum. Methods A **524**, 102 (2004).
86. R.L. Macklin *et al.*, Nucl. Instrum. Methods **164**, 213 (1979).
87. J. Balibrea *et al.*, Nucl. Data Sheets **119**, 10 (2014).
88. F. Belloni *et al.*, Mod. Phys. Lett. A **28**, 1340023 (2013).
89. D. Tarrio *et al.*, Nucl. Instrum. Methods A **743**, 79 (2014).
90. P. Žugec *et al.*, Phys. Rev. C **90**, 021601 (2014).
91. P. Žugec *et al.*, Eur. Phys. J. A **52**, 101 (2016).
92. C. Massimi *et al.*, Nucl. Data Sheets **119**, 110 (2014).
93. C. Massimi *et al.*, submitted to Phys. Lett. B (2016).
94. M. Sabat-Gilarte *et al.*, Rep. Pract. Oncol. Radiother. **21**, 113 (2016).
95. G. Giubrone *et al.*, Nucl. Data Sheets **119**, 117 (2014).
96. P. Žugec *et al.*, Phys. Rev. C **89**, 014605 (2014).
97. C. Weiss *et al.*, Nucl. Data Sheets **120**, 208 (2014).
98. C. Lederer *et al.*, Phys. Rev. C **89**, 025810 (2014).
99. C. Lederer *et al.*, Phys. Rev. Lett. **110**, 022501 (2013).
100. F. Gunsing *et al.*, Nucl. Data Sheets **119**, 132 (2014).
101. G. Tagliente *et al.*, Phys. Rev. C **87**, 014622 (2013).
102. D. Tarrio *et al.*, Nucl. Data Sheets **119**, 35 (2014).
103. E. Leal-Cidoncha *et al.*, EPJ Web of Conferences **111**, 10002 (2016).
104. C. Paradela *et al.*, EPJ Web of Conferences **111**, 02003 (2016).
105. M. Barbagallo *et al.*, Nucl. Data Sheets **119**, 45 (2014).
106. F. Mingrone *et al.*, Nucl. Data Sheets **119**, 18 (2014).
107. T. Wright *et al.*, Nucl. Data Sheets **119**, 26 (2014).
108. A. Tsinganis *et al.*, Nucl. Data Sheets **119**, 58 (2014).
109. K. Fraval *et al.*, Phys. Rev. C **89**, 044609 (2014).
110. E. Mendoza *et al.*, Nucl. Data Sheets **119**, 65 (2014).
111. E. Chiaveri *et al.*, Technical report (2011).
112. S. Lo Meo *et al.*, Eur. Phys. J. A **51**, 160 (2015).
113. J. Lerendegui-Marco *et al.*, Eur. Phys. J. A **52**, 100 (2016).
114. L. Cosentino *et al.*, Rev. Sci. Instrum. **86**, 073509 (2015).
115. L. Cosentino *et al.*, Nucl. Instrum. Methods A **830**, 197 (2016).
116. A. Tsinganis *et al.*, in *14th Int. Conf. Nucl. Reac.*, edited by F. Cerutti *et al.* (CERN-Proc.-2015-001, 2015) pp. 21–26.
117. J. Lerendegui-Marco *et al.*, EPJ Web of Conferences **111**, 02005 (2016).
118. G. Tagliente *et al.*, in *14th Int. Conf. Nucl. Reac.*, edited by F. Cerutti *et al.* (CERN-Proc.-2015-001, 2015) pp. 267–274.
119. A.J. Pollitt *et al.*, EPJ Web of Conferences **93**, 02018 (2015).
120. H. Derrien *et al.*, Nucl. Sci. Eng. **160**, 149 (2008).
121. I. Sirakov *et al.*, Ann. Nucl. Energy **35**, 1223 (2008).
122. `https://www.oecd-nea.org/dbdata/hprl`.
123. M.B. Chadwick *et al.*, Nucl. Data Sheets **118**, 1 (2014).
124. B. Becker *et al.*, J. Instrum. **7**, P11002 (2012).
125. C. Sage *et al.*, Phys. Rev. C **81**, 064604 (2010).
126. X. Ledoux *et al.*, Ann. Nucl. Energy **76**, 514 (2015).
127. F. Gunsing *et al.*, Technical Report IAEA INDC(NDS)-0647 (2013).
128. `http://twiki.cern.ch/NTOFPublic`.
129. M. Barbagallo *et al.*, Phys. Rev. Lett. **117**, 152701 (2016).